Chemical Engineering Journal 527 (2026) 171840

Contents lists available at ScienceDirect

Chemical Engineering Journal

journal homepage: www.elsevier.com/locate/cej

Oxygen vacancy-rich Ti (sub)oxide electrodes boost desalination performance on hybrid capacitive deionization (HCDI) platforms

Pengcheng Yin [a], Yucheng Yang [a], Shu Zhang [a], Zhao Hu [b], Dawei Li [a], Feihu Li [a,c,*]

[a] Collaborative Innovation Center of Atmospheric Environment and Equipment Technology, Jiangsu Key Laboratory of Atmospheric Environment Monitoring and Pollution Control, School of Environmental Science and Engineering, Nanjing University of Information Science and Technology, 219 Ningliu Road, Nanjing 210044, China

[b] Changwang School of Honors, Nanjing University of Information Science and Technology, 219 Ningliu Road, Nanjing 210044, China

[c] NUIST Reading Academy, Nanjing University of Information Science and Technology, 219 Ningliu Road, Nanjing 210044, China

ARTICLE INFO

Keywords:
Titanium (sub)oxides
Electrode materials
Oxygen vacancy
Capacitive deionization

ABSTRACT

The potential of capacitive deionization (CDI) for sustainable desalination depends critically on breakthroughs in electrode materials. Defect-rich titanium (sub) oxides (anatase TiO_2(A), Ti_2O_3, Ti_3O_5, Ti_4O_7) offer compelling advantages, including tunable capacity, low environmental impact, and robustness. This study provides a systematic comparison of their structural features, electrochemical responses, and desalination efficacy. Electrochemical characterization results show anatase TiO_2(A) leads in specific capacitance (252.5 F g^{-1} at 0.3 A g^{-1}), while Ti_3O_5's highest oxygen vacancy minimizes charge transfer resistance and maximizes ion migration rates. In desalination trials, TiO_2 delivers a maximum salt adsorption capacity of 37.1 mg g^{-1} (500 mg L^{-1} NaCl, 1.2 V). All electrodes exhibit outstanding cycling stability (capacity retentions >83.5 %), affirming their practical potential. Correlation analysis discloses the oxygen vacancy-driven charge transfer mechanism inside these electrodes and establishes a structure-performance relationship. Overall, this work establishes fundamental structure-property relationships that underpin future electrode innovation via the oxygen vacancy-engineering strategy, which represents a promising pathway for advancing CDI performance boundaries.

1. Introduction

The global water resources are currently facing unprecedented challenges. Climate change leads to frequent extreme weather events, exacerbating the uneven distribution of water resources and causing some regions to suffer from increased drought while others experience frequent floods [1]. Meanwhile, the continuous growth of the global population has further amplified the demand for freshwater, leaving many regions severely water-stressed [2]. To address the pressing global challenge of water scarcity, the development of energy-efficient and cost-effective desalination technologies has become increasingly imperative [3]. Recently, capacitive deionization (CDI) has emerged as a promising energy-efficient desalination alternative to the traditional seawater desalination technologies such as reverse osmosis (RO), electrodialysis (ED), multi-stage flash distillation (MSF), multi-effect distillation (MED), and mechanical vapor compression (MVC), which usually suffered from issues including high capital investment, high energy consumption, high operational costs, and equipment scaling and/or corrosion [4–6]. The basic principle of CDI can be simply described as the electrosorption of ions onto porous carbon electrode surfaces driven by the electrostatic field between the two parallel electrodes [7,8]. The practical application of conventional CDI is inherently constrained by its fundamental operational principles, which result in a low salt adsorption capacity (SAC) dictated by the electrical double-layer (EDL) capacitance of porous carbon and an inefficient charging phase due to the co-ion expulsion effect [7,9]. These drawbacks prompt the development of the superior Hybrid Capacitive Deionization (HCDI) architecture, which uniquely combines a capacitive carbon electrode with a Faradaic electrode that undergoes reversible redox reactions [10]. This synergistic combination enables ion storage via both electrosorption and faradaic processes, leading to significantly enhanced SAC and energy efficiency [9–12]. The performance of an HCDI system is predominantly

* Correspnding author at: Collaborative Innovation Center of Atmospheric Environment and Equipment Technology, Jiangsu Key Laboratory of Atmospheric Environment Monitoring and Pollution Control, School of Environmental Science and Engineering, Nanjing University of Information Science and Technology, 219 Ningliu Road, Nanjing 210044, China.
E-mail address: fhli@nuist.edu.cn (F. Li).

https://doi.org/10.1016/j.cej.2025.171840
Received 22 October 2025; Received in revised form 5 December 2025; Accepted 11 December 2025
Available online 12 December 2025

governed by the intrinsic properties (i.e., kinetics, capacity, and stability) of its Faradaic electrode [13–15]. This direct correlation establishes a fundamental rationale for the focused development of advanced Faradaic materials to push the boundaries of efficient desalination technology.

HCDI platforms leverage Faradaic materials to enhance the electrochemical desalination of brackish water. Typical electrode materials include manganese oxide, layered metal oxide nanosheet, silver-based compounds, and conducting polymers like polyaniline [15–21]. While these materials offer high theoretical capacity or favorable kinetics, they are plagued by significant shortcomings that impair their desalination performance. For instance, manganese oxide suffers from Mn dissolution in aqueous electrolytes, leading to rapid performance decay [12,14,22]. Silver-based materials, though highly conductive, are prohibitively expensive and prone to electrochemical corrosion [23,24]. Conducting polymers, while synthetically tunable, undergo substantial volumetric swelling and shrinking during ion insertion/extraction, resulting in mechanical degradation and poor long-term stability [25,26]. In this context, titanium oxides have emerged as promising alternatives to Faradaic electrode materials for HCDI, offering inherent stability, low cost, and environmental friendliness [27–29]. Consequently, most research efforts have been directed specifically toward titanium dioxide (TiO_2) and its carbon composites [27–31]. For instance, TiO_2 exhibits excellent electrochemical stability [32] and a relatively high theoretical capacity [29,33], especially in its anatase phase [34], which shows outstanding performance in ion storage [35]. Nanostructured TiO_2 provides abundant active sites, facilitating efficient transport of electrons and ions, thus enhancing the electrode's capacitance and response speed [36]. In addition, the charged surface of TiO_2 effectively reduces electrode polarization, with enhanced adsorption capacity and improved desalination efficiency [37]. However, while TiO_2 boasts excellent chemical and electrochemical stability, its practical application is often constrained by intrinsically poor electronic conductivity [38,39]. This limitation reveals a critical research gap: a systematic and comparative investigation of the entire family of titanium suboxides—the Magnéli phases (Ti_nO_{2n-1})—for HCDI applications is severely lacking [40–42]. For instance, Ti_4O_7, a typical Magnéli phase titanium suboxide [43], demonstrates a high electronic conductivity, superior electrochemical performance and desalination advantages [44,45]. While these sub-stoichiometric oxides exhibit metallic-like conductivity and higher theoretical capacities owing to their crystallographic shear planes and oxygen deficiency, the fundamental relationship between their distinct oxygen vacancy (O_v) concentrations and their ultimate desalination performance remains virtually unexplored and poorly understood [41,42]. Addressing this knowledge gap is essential for the rational design of high-performance titanium oxide electrodes.

To this end, this work presents a comprehensive study exploring a suite of oxygen vacancy-rich titanium (sub)oxides (i.e., anatase TiO_2 (denoted as TiO_2(A)), Ti_2O_3, Ti_3O_5, and Ti_4O_7) as electrodes on an HCDI platform, with emphasis on the relationship between their O_v concentrations and the key desalination performance metrics. This graded series of titanium (sub)oxides provides a proper platform to fundamentally investigate how critical electronic properties (metallic vs. semiconducting behavior), and O_v concentrations collectively govern the SAC, rate capability, and cycling stability in HCDI systems. This approach directly addresses the intrinsic limitations of conventional TiO_2, namely its poor electronic conductivity, paving the way for high-performance HCDI electrodes.

This study aims to elucidate how variations in crystal structure and defect characteristics govern titanium (sub)oxide electrodes for efficient desalination. Specific objectives include characterizing a graded series of titanium (sub)oxides (TiO_2(A), Ti_2O_3, Ti_3O_5, Ti_4O_7) to rigorously confirm their phase purity, morphology, and critically, their distinct O_v densities [46,47]. These materials will be electrochemically evaluated in a three-electrode configuration to quantify key parameters, including capacitance and charge transfer resistance. Their desalination performance was systematically assessed within a hybrid CDI cell, employing nitrogen-doped activated carbon (NAC) as the counter electrode. Leveraging its excellent electrical conductivity and surface activity, the NAC works synergistically with the titanium (sub)oxide electrodes (e.g., TiO_2(A)//NAC) to enhance their overall electrochemical properties and desalination efficiency. Finally, the electrochemical behavior and desalination performance were directly correlated with the intrinsic material properties—specifically O_v concentration—to establish a definitive structure-property-performance relationship for titanium (sub)oxide electrodes.

2. Materials and methods

2.1. Chemicals

Titanium dioxide (anatase, TiO_2(A)) and titanium suboxide (Ti_2O_3) were purchased from Macklin Chemical Co., Ltd. Ti_3O_5 was purchased from Tianyuan-Ye Biotech Co., Ltd., while Magnéli Ti_4O_7 powder with a particle size ranging from 5 to 15 μm was obtained from Hunan Kelai New Materials Co., Ltd. (China). Sodium chloride (NaCl), activated carbon (AC), ammonium hydroxide (NH_4OH), carbon black (CB), and polyvinylidene fluoride (PVDF) were obtained from Aladdin Chemical Co. All chemicals were used as received. Ultrapure deionized water (DI H_2O, 18.2 Ω cm at 25 °C) was used for preparing solutions.

2.2. Preparation of nitrogen-doped activated carbon

Following a well-established ball-milling protocol [48], nitrogen-doped activated carbon (NAC) was facilely prepared and employed as the counter electrode of the HCDI cell. Briefly, 1.8 g of activated carbon and 18 mL of ammonium hydroxide (29 %) were loaded into a ball milling jar, sealed, and fixed onto a planetary ball mill. The mixture was milled at a speed of 300 rpm for 12 h, with the rotation direction changed every 3 h. Subsequently, the product was washed with deionized water using a vacuum filtration setup, and the solid residue on the filter was dried in an oven at 80 °C for 48 h. After cooling down to room temperature, the obtained NAC powder was collected and stored in a glass desiccate for further use.

2.3. Materials characterization and electrochemical measurements

The crystal phases of all samples were analyzed by X-ray diffraction (XRD) using a Shimadzu XRD-6100 X-ray diffractometer with Cu-Kα radiation at a tube voltage of 40 kV and a tube current of 30 mA. The microscopic morphology was recorded on a Gemini 300 field emission scanning electron microscope (ZEISS, Germany). Fourier transform infrared (FTIR) spectroscopy was performed on a Nicolet iS5 infrared spectrometer (Thermo Fisher, USA) using the KBr pellet method. X-ray photoelectron spectroscopic (XPS) data were obtained with an electron spectrometer (UIVAC-PHI, Japan) using 300 W Al Kα radiation, with the adventitious carbon species C 1 s (284.8 eV) for binding energy (BE) correction. The O 1 s regional peak can be deconvoluted into three components: the lattice oxygen (O_L) at 529.0–530.5 eV, the oxygen vacancy (O_V) at 530.5–531.7 eV, and the surface adsorbed oxygen/species (O_S) at 531.8–532.8 eV. The relative O_V concentration ([Ov]) was then estimated from the peak area ratio of $O_V/(O_L + O_V)$ [49]. X-band Electron Paramagnetic Resonance (EPR) spectra were recorded by a Bruker EMX spectrometer (ESR 5000).

2.4. Electrochemical measurements

All electrochemical measurements were carried out in 1.0 M NaCl solution with a three-electrode system (platinum foil as counter electrode, Ag/AgCl as reference electrode, and titanium (sub)oxides as working electrode) on a CS310H electrochemical workstation (Correst

Instruments Inc., China) at ambient temperature [50]. The working electrodes were prepared by combining titanium (sub)oxides, carbon black, and polyvinylidene fluoride (PVDF) in a mass ratio of 8:1:1. The mixture was then dispersed and ground in an agate mortar using 1-methyl-2-pyrrolidone as dispersant until a homogeneous slurry was obtained. The slurry was sequentially applied onto a clean graphite paper (1 cm × 1 cm), which was dried in a vacuum at 80 °C for 2 h, and then used as the working electrode. Cyclic voltammetry (CV) was performed at a scan rate of 5–100 mV s^{-1}. Galvanostatic charge-discharge (GCD) analysis was conducted at a current density of 0.3–2 A g^{-1}. Electrochemical impedance spectroscopy (EIS) measurement was examined at a frequency of 10^{-5}–0.01 Hz, and the applied bias voltage and ac amplitude were set at open-circuit potential and 5 mV, respectively. The specific gravimetric capacitance of the electrode was calculated by Eq. (1),

$$C_s = \frac{I \times \Delta t}{m \times \Delta V} \tag{1}$$

where C_s is the specific capacitance determined by GCD discharge curves (F g^{-1}), m stands for the mass of the active materials in the electrode (g), I refers to the discharge current (A), Δt is the discharge time (s), and ΔV represents the potential window of the discharge (V).

2.5. Capacitive deionization test

Following the same protocol described earlier [12], the electrodes (30 mg in mass, ~ 30 μm in thickness, 8:1:1 of titanium (sub)oxides: carbon black: PVDF) for CDI tests were prepared on a 5 cm × 5 cm graphite paper [51] and then assembled into a homemade HCDI cell (Fig. S1, Supplementary data). The CDI tests were performed in batch mode under constant voltage conditions with a total volume of feed solution of 30 mL. By convention, voltages of 0.8–1.2 V and feed solutions of 100–500 ppm NaCl solutions were used to examine the effects of cell voltage and feed solution concentration on the CDI performance, respectively. The salt adsorption capacity (SAC, Γ) of the electrode was determined using Eq. (2),

$$\Gamma = \frac{(C_0 - C_e)V}{m} \tag{2}$$

where C_0 and C_e are the initial and the final concentration of the feed solution (mg L^{-1}), respectively, V is the solution volume (mL), and m refers to the mass of the active electrode material on one side (g).

The charge efficiency (Λ, %) was calculated according to Eq. (3),

$$\Lambda = \frac{SAC \times F}{M \times \sum} \tag{3}$$

where F is the Faraday constant (96,485 C mol^{-1}), Σ refers to the total charge associated with the integrated corresponding current (C g^{-1}), and M (g mol^{-1}) is the molar weight of the target ion.

3. Results and discussions

3.1. Physicochemical characteristics of the titanium (sub)oxides

The titanium (sub)oxides examined in this study exhibit a well-defined progression in crystal structure and stoichiometry (Fig. 1a), directly corresponding to their theoretical oxygen vacancy (O_v) concentrations. Specifically, TiO_2(A) possesses a body-centered tetragonal structure ($I4_1/amd$), serving as the reference point with a theoretical O_v concentration of zero per Ti atom [46]. In contrast, the suboxides Ti_2O_3 (rhombohedral, R-3c), Ti_3O_5 (monoclinic, C2/m), and Ti_4O_7—the latter a member of the Magnéli phases (Ti_nO_{2n-1}) with a triclinic P-1 space group—demonstrate increasing structural complexity and theoretically possess 0.5, 0.333, and 0.25 oxygen vacancies per Ti atom, respectively, relative to the TiO_2 lattice (Text S1, Supplementary data) [52]. XRD

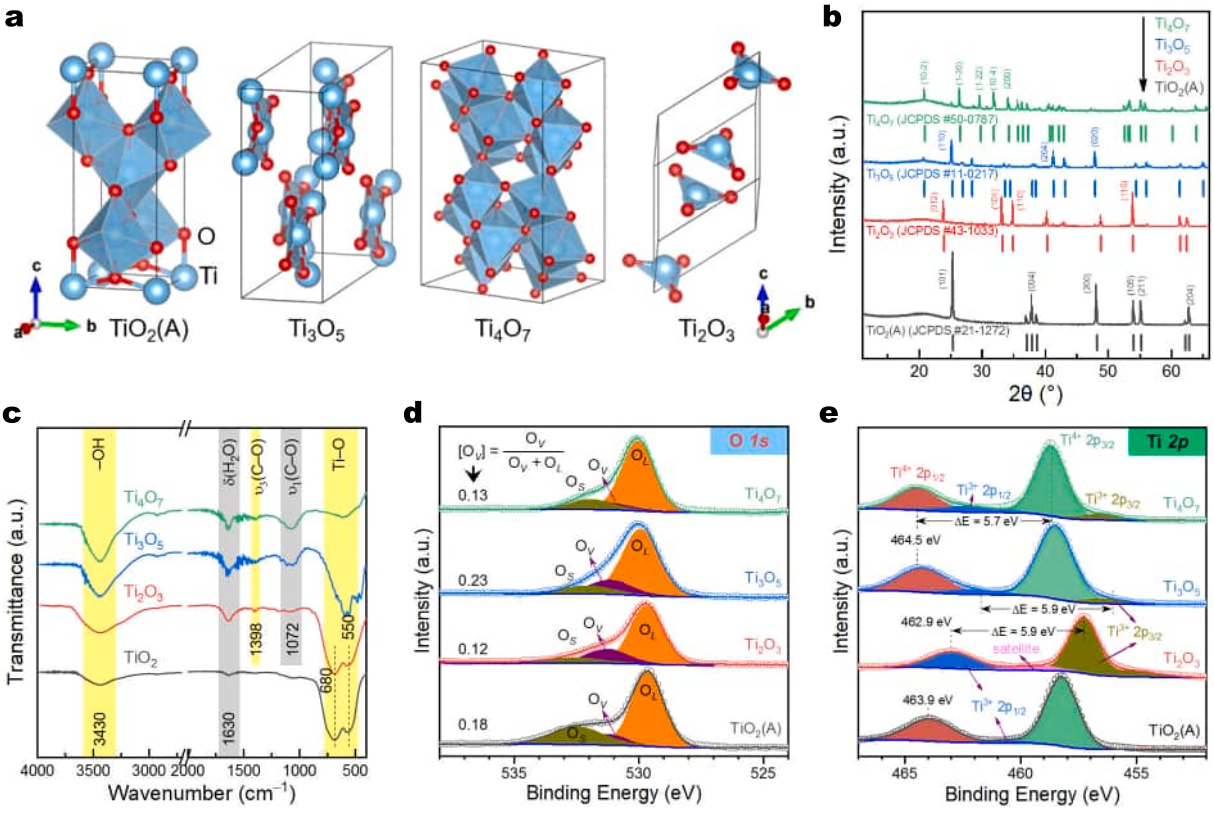

Fig. 1. (**a**) Crystal structures, (**b**) XRD patterns, (**c**) FTIR, and (**d-e**) XPS spectra of O 1 s (**d**) and Ti 2p (**e**) regions of the titanium (sub)oxides. Note the relative concentration of oxygen vacancies ([O_V]) calculated from the ratio of $O_V/(O_V + O_L)$ is given for each sample in panel **d**.

analysis confirms the high phase-purity and crystallinity of these materials, as the major reflections for anatase TiO_2(A) at 25.3° (101), 37.8° (004), and 48.0° (200), among others, align perfectly with the standard JCPDS card #21–1272 (Fig. 1b). Similarly, the sharp, well-defined diffraction patterns for Ti_2O_3, Ti_3O_5, and Ti_4O_7 display no evidence of interfering phases and match their respective JCPDS standards (#43–1033, #11–0127, and #50–0787), confirming monophasic compositions with distinct crystal structures [53,54].

Complementary spectroscopic techniques provide direct evidence of the surface chemistry and electronic states derived from these oxygen deficiencies, with XPS offering particularly profound insights into the quantitative and qualitative nature of these defects [46]. FTIR spectroscopy reveals not only the expected Ti—O stretching vibrations between 500 and 700 cm^{-1} and hydroxyl group signals from adsorbed water (3430 and 1630 cm^{-1}) [55], but also prominent symmetric (ν_1, 1072 cm^{-1}) and asymmetric (ν_3, 1398 cm^{-1}) vibrations attributable to surface carbonate species (Fig. 1c) [56]. The presence of these C—O groups is a direct consequence of the high concentration of O_V, which generates highly reactive surface sites that readily chemisorb and transform atmospheric CO_2, thereby passivating the surface and forming stable carbonaceous deposits [57]. This interpretation is further supported by XPS spectroscopy (Figs. 1d-e and S2a,b). Specifically, the deconvolution of the O 1 s regional spectra reveals a nuanced picture of the surface oxygen chemistry. The O 1 s spectra were deconvoluted into three components: the lattice oxygen (O_L) at ~529.6 eV, the oxygen vacancy (O_V) at ~530.9 eV, and the surface adsorbed oxygen species

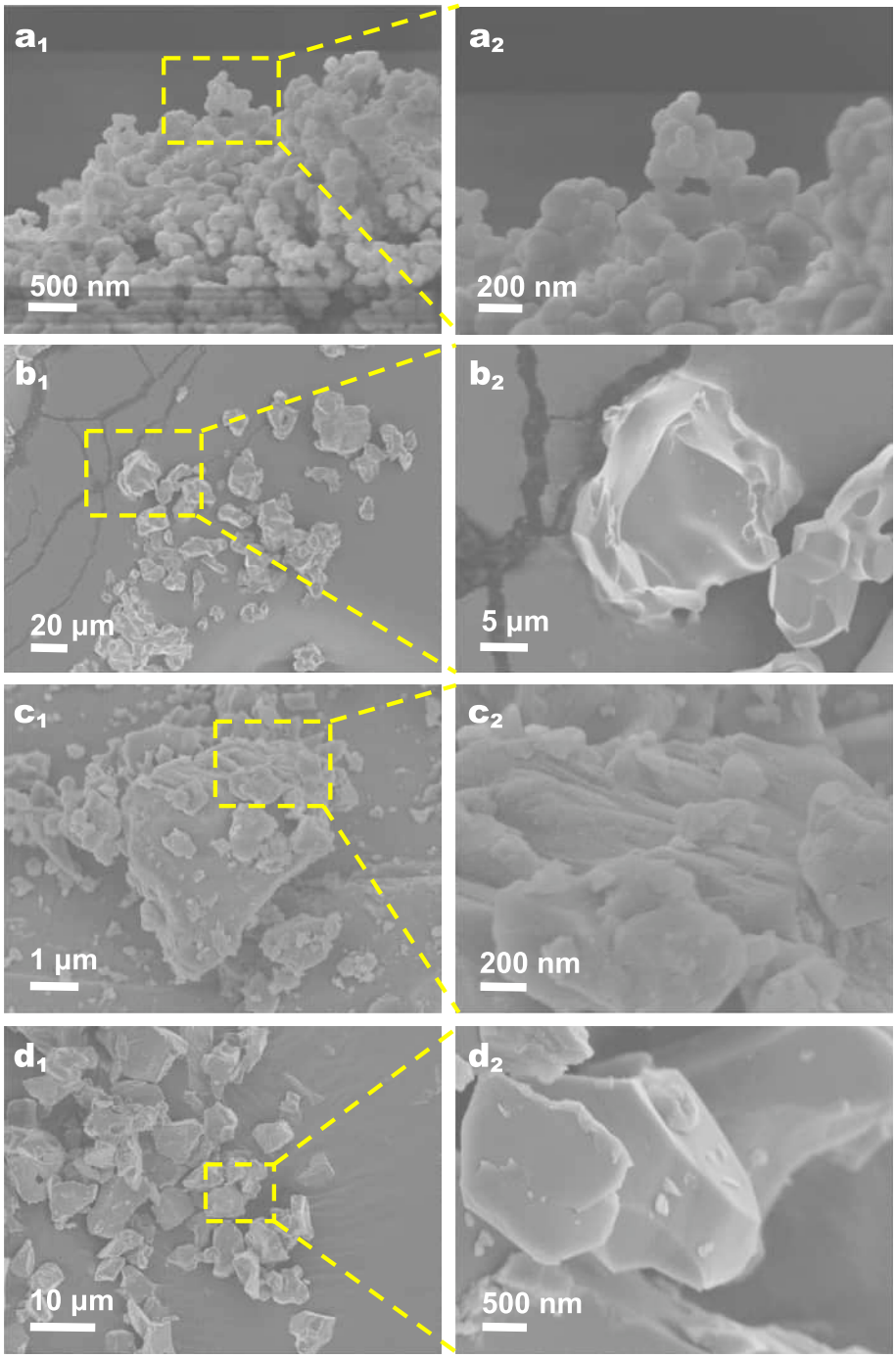

Fig. 2. SEM images of titanium (sub)oxides at varying magnification levels: (**a**$_1$, **a**$_2$) TiO_2(A), (**b**$_1$, **b**$_2$) Ti_2O_3, (**c**$_1$, **c**$_2$) Ti_3O_5, and (**d**$_1$, **d**$_2$) Ti_4O_7.

(O_S) at ~532.5 eV (Fig. 1d). The relative concentration of oxygen vacancies ([Ov]) was estimated from the peak area ratio of $O_V/(O_L + O_V)$ [49,58]. The measured [Ov] concentrations of 0.18, 0.12, 0.23, and 0.13 for TiO_2(A), Ti_2O_3, Ti_3O_5, and Ti_4O_7, respectively (Fig. 1d), present a fascinating deviation from the theoretical bulk values. The presence of a measurable O_V signal (0.18) in nominally stoichiometric TiO_2(A) is indicative of inherent surface defects and underscores the sensitivity of XPS to surface, rather than bulk composition. Complementary EPR spectra also confirmed these intrinsic O_V species associated with anatase Ti^{3+} interstitials ($g_1 = 1.999$, $g_\perp = 1.99$, $g_\parallel = 1.965$ and $g_2 = 1.934$, Fig. S2c) [59]. The unexpectedly low value for Ti_2O_3 (0.12 vs. 0.5 theoretical) suggests a surface passivation effect, where the highly reduced Ti^{3+} sites at the surface are readily oxidized by ambient air, effectively reducing the detectable O_V population and forming a thin, TiO_2-like overlayer [46]. Conversely, the significantly higher O_V concentration in Ti_3O_5 (0.23) highlights its structurally stabilized, high-density defect nature, which appears robust even at the surface [47]. This quantitative analysis is unequivocally corroborated by the chemical state information derived from the Ti 2p regional spectra. Specifically, deconvolution of the Ti 2p XPS spectra confirms the expected oxidation states: Ti^{4+} dominates in TiO_2(A) as evidenced by the ΔE of 5.7 eV, Ti^{3+} in Ti_2O_3 with ΔE of 5.9 eV, and a mixed Ti^{3+}/Ti^{4+} state in both Ti_3O_5 and Ti_4O_7 (Fig. 1e). The consistency between the O 1 s and Ti 2p spectral data unequivocally signifies the presence of oxygen vacancies across all the titanium (sub)oxides, linking their crystallographic structure directly to their surface reactivity and electronic properties [52,60].

Fig. 2 presents the morphologies of the titanium (sub)oxides. TiO_2(A) sample exhibits a semi-spherical cluster structure with uniformly distributed fine particles (Fig. 2a). Its hierarchical structure is evident by the inter-particle connections of TiO_2 nanoparticles with rough surfaces, which is beneficial for facilitating interfacial electron and ion transport and thereby improving the electrochemical performance. The suboxide Ti_2O_3 is featured by micro-sized particles with sharp edges (Fig. 2b), signifying its high crystallinity and integrity. This is in good agreement with the XRD data (Fig. 1b). Likewise, Ti_3O_5 appears as irregular particles of diverse distribution (Fig. 2c); the tight inter-particle bonding may contribute to enhanced electrical conductivity and structural stability. Similarly, the Magnéli phase Ti_4O_7 dominates a mixture of irregular particles with well-defined edges and smooth surfaces (Fig. 2d), implying its high crystallinity (Fig. 1b). In addition, the morphological features of these titanium (sub)oxides are in good consistency with earlier reports [47,61], confirming their phase purity as examined by XRD.

3.2. Electrochemical properties of electrodes

The electrochemical properties of these titanium (sub)oxide (TiO_2(A), Ti_2O_3, Ti_3O_5, and Ti_4O_7) electrodes were comprehensively evaluated by CV, GCD, and EIS with a three-electrode system in 1.0 M NaCl solution. Fig. 3a presents the CV curves of these titanium (sub) oxide electrodes measured at a scan rate of 5 mV s^{-1}. Generally, an ideal rectangular CV curve indicates that the electrode material exhibits pure electric double-layer capacitance (EDL) behavior, while quasi-rectangular curves or pronounced redox peaks reflect pseudocapacitive effects [7,19,23]. Mixed-type curves demonstrate that the material possesses both EDL and pseudocapacitive characteristics [17,26]. The CV curves in Fig. 3a demonstrate synergistic EDL and pseudocapacitive behavior across all titanium (sub)oxide electrodes. This synergy results from their inherent electrochemical activity and surface characteristics [53,61]. Specifically, the pseudocapacitive contribution involves

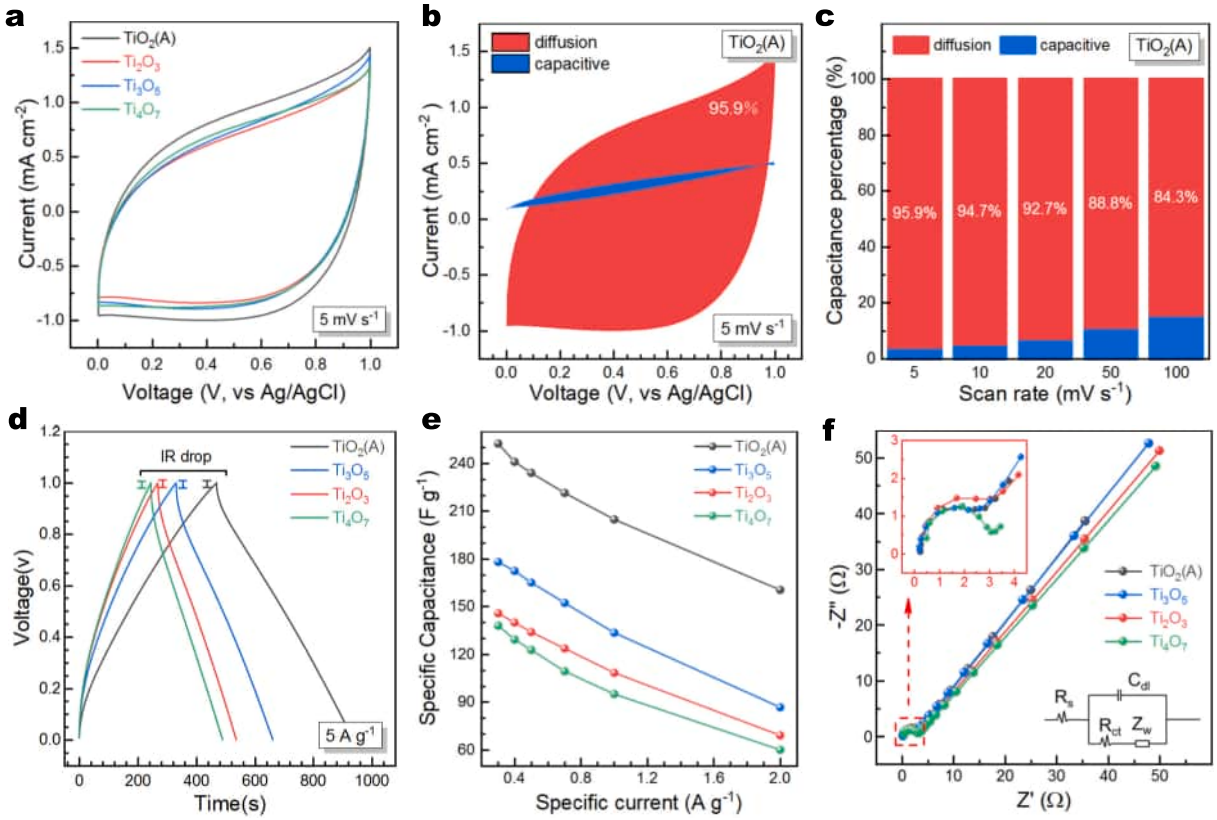

Fig. 3. Electrochemical characterizations of titanium (sub)oxide electrodes in 1.0 M NaCl solution: (**a**) CV curves at 5 mV s^{-1}; (**b**) capacitive- and diffusion-controlled contribution to the charge storage of TiO_2(A) at 5 mV s^{-1}; (**c**) contribution ratios of capacitive- and diffusion-controlled capacity for TiO_2(A) at different scan rates; (**d**) GCD curves at 5 A g^{-1}; (**e**) specific capacitances at different specific currents; and (**f**) Nyquist curves of EIS and the fitting curves obtained in 1.0 M NaCl with a frequency of 10–5–0.01 Hz and an ac amplitude of 5 mV, inset on the bottom right is the equivalent circuit.

reversible Na^+ insertion/extraction and concurrent Ti^{4+}/Ti^{3+} redox reactions (Figs. 3a, S3) [17,36]. Notably, the anatase TiO_2(A) electrode shows the largest integration area under the CV curve (Fig. 3a), denoting the highest specific capacitance (C_s) and ion storage capacity among the tested electrodes [14]. Furthermore, all titanium (sub)oxide electrodes demonstrate excellent reversibility (0–1.0 V) with minimal current drift, confirming stable structures and cycling stability [36].

To further understand the capacitive and ion diffusion behaviors of the titanium (sub)oxide electrodes, we calculated the non-diffusion (capacitive) and diffusion-controlled contribution (Text S2) based on their voltammetric scan rate dependence (Fig. S3). For instance, anatase TiO_2(A) shows diffusion-dominated charge storage (95.9 %) at 5 mV s^{-1}, with capacitive contribution at 4.1 % (Fig. 3b). Increasing the scan rate up to 100 mV s^{-1} significantly enhances capacitive contribution to 15.7 % (Fig. 3c). This performance stems from its efficient charge transport and rapid Na^+ diffusion, facilitated by its open crystal structure and abundant oxygen vacancies [47]. While other titanium (sub)oxides show analogous trends, their capacitive contributions increase less markedly (Figs. S3–S6) and remain predominantly diffusion-controlled. The overall capacitive enhancement at higher scan rates across all materials is attributed to kinetic limitations in Na^+ diffusion or intercalation [26].

GCD curves (Fig. 3d) reveal asymmetric charge-discharge profiles for all titanium (sub)oxide electrodes at 0.5 A g^{-1}, deviating from ideal triangular symmetry. This observation indicates pseudocapacitive reactions and Faradaic charge storage behavior beyond EDL mechanisms [17,26], aligning with CV observations (Fig. 3a) and confirming reversible Ti^{4+}/Ti^{3+} redox in all electrodes. Notably, anatase TiO_2(A) shows the longest discharge plateau among all electrodes (Figs. S8a-d), suggesting enhanced charge storage capability and electrochemical performance – corroborating with its CV data (Fig. 3a). Note that the C_s values of titanium (sub)oxide electrodes, derived from GCD discharge curves (beyond iR drop, eq. 1), declines with increasing current density (0.3–2.0 A g^{-1}) (Fig. 3e). Anatase TiO_2(A) achieves the highest C_s (252.5 F g^{-1} at 0.3 A g^{-1}), outperforming Ti_2O_3 (145.9 F g^{-1}), Ti_3O_5 (178.1 F g^{-1}), and Ti_4O_7 (138.0 F g^{-1}) (Table S1). This superior ion storage stems from pseudocapacitive effects inherent to its structure, amplified by its finer grain composition and optimized interfacial ion channels (Fig. 2a) [62]. Additionally, the anatase TiO_2(A) also maintains robust rate performance with minimal capacitance fade at high currents, alongside a significantly reduced *i*R drop (Fig. S8e), indicative of low charge-transfer resistance. These results confirm anatase TiO_2(A) as the superior electrode for high-performance ion storage compared to other titanium suboxide electrodes.

Nyquist plots (Fig. 3f) reveal a small semicircle in the high-frequency region and a steep Warburg tail in low/medium frequencies for all electrodes. The semicircle diameter corresponds to charge-transfer resistance (R_{ct}) at the electrode/electrolyte interface. Fitting data to the equivalent circuit (inset, Fig. 3f) yields comparable R_{ct} values of 2.2 Ω (TiO_2(A)), 2.49 Ω (Ti_2O_3), 2.09 Ω (Ti_3O_5), and 2.46 Ω (Ti_4O_7) (Table S1). The Ti_3O_5 electrode exhibits the smallest semicircle (R_{ct} = 2.09 Ω), indicating superior electron transfer. Warburg impedance (Z_w)—derived from the mid-to-low-frequency slope—follows the trend: $Ti_4O_7 \approx Ti_2O_3 < TiO_2$(A) $\approx Ti_3O_5$ (Table S1), confirming Ti_4O_7's fastest interfacial ion migration [39,40]. Notably, the Ti_3O_5 electrode exhibits exceptional electron transfer and interfacial ion transport performance rivaling Ti_4O_7. This superiority arises from its Magnéli phase architecture and high O_V concentration ($[O_V]$ = 0.23, Fig. 1d), which synergistically boost electronic conductivity and facilitate rapid ion diffusion via oxygen vacancy pathways [62]. Recall that the anatase TiO_2(A) demonstrates the maximum ion storage capacity (Fig. 3a, e) and intrinsic oxygen vacancy ($[O_V]$ = 0.13, Fig. 1d). These results collectively establish anatase TiO_2(A) as the optimal electrode for superior electrochemical performance and ion storage.

3.3. Performance of capacitive deionization

Initially, the desalination performance of all these titanium (sub) oxide electrodes was tested in a 100 mg L^{-1} of NaCl solution under a constant voltage of 1.2 V on an HCDI platform employing titanium (sub) oxide and NAC as the electrode pair (e.g., TiO_2(A)//NAC). Typically, the conductivity vs. time curves show two distinct stages (Fig. 4a): the charging stage where Na^+ ions are intercalated into the titanium (sub) oxide electrodes driven by the electric field and the conductivity of solution gradually decreases (yellow shaded area); and the discharging stage where Na^+ ions desert from the electrodes, and the conductivity gradually reclaims (cyan shaded area), both stages together constitute a complete adsorption-desorption cycle [7,8]. For instance, the TiO_2(A) electrode demonstrates sharp conductivity decreases in the charging stage and rapid recovery upon discharging (Fig. 4a), indicating efficient Na^+ capture and release. This behavior stems from its open, and regular [TiO_6] octahedral structure with oxygen vacancies (Fig. 1a) [46,63], which forms unique ion diffusion channels enabling facile Na^+ (de) intercalation. Concurrently, synergistic electronic-ionic transport facilitates rapid charge transfer, allowing swift Na^+ (de)intercalation. These observations align with the CV and GCD results (Fig. 3a, d). Ti_4O_7 and Ti_3O_5 show comparable conductivity trends due to their Magnéli phase nature—characterized by abundant oxygen vacancies and metallic conductivity [53]. However, their compact crystal structures and limited Na^+ intercalation sites [52,61] restrict storage capacity, resulting in inferior performance versus TiO_2(A). Ti_2O_3's denser structure and lower porosity severely impede Na^+ diffusion, compounded by weak electronic conductivity [53], leading to slow conductivity changes and poor desalination (Fig. 4a). Quantitatively, TiO_2(A) achieves the highest Γ (17.2 mg g^{-1} in 100 mg L^{-1} of NaCl solution, at 1.2 V), outperforming Ti_4O_7 (16.6 mg g^{-1}), Ti_3O_5 (16.4 mg g^{-1}), and Ti_2O_3 (11.2 mg g^{-1}) (Fig. S9a).

As anticipated, the corresponding charging current decreases uniformly across all electrodes (Fig. 4b), with charge efficiencies (Λ) ranking as follows: TiO_2(A) (0.49) > Ti_4O_7 (0.33) ≈ Ti_3O_5 (0.31) > Ti_2O_3 (0.26). The TiO_2(A) electrode achieves the highest Λ, attributable to its open crystal structure and synergistic ion-electron transport mediated by O_V [62,63]. Notably, the non-composite TiO_2(A) electrode demonstrates a much lower Λ compared with other TiO_2/carbon composite electrodes, primarily due to its intrinsic semiconductor nature [33]. Conversely, the minimal Λ value of Ti_2O_3 is severely constrained by its dense lattice and poor electronic conductivity [53]. Though Ti_3O_5 and Ti_4O_7 exhibit high adsorption rates, their lower Λ (vs. TiO_2(A)) stems from structural and interfacial limitations (e.g., denser structure with fewer, more constrained cavities for accommodating Na^+ [53] and larger particle sizes and agglomeration in relative to TiO_2(A), Fig. 2). Kim-Yoon analysis (***SAR*** vs. Γ, Fig. 4c) further clarifies performance trade-offs: Ti_3O_5 and Ti_4O_7 outperform at low-to-medium Γ (1–10 mg g^{-1}), leveraging oxygen vacancies for rapid Na^+ diffusion and uptake. Yet their adsorption capacity plateaus at higher loadings, unlike TiO_2(A)—whose open crystal structure and larger theoretical capacity enable sustained, high-efficiency operation across all Γ ranges.

To assess the desalination performance of titanium (sub)oxide electrodes under varying conditions, we investigated the effects of cell voltage (0.8–1.2 V in 100 mg L^{-1} NaCl) and feed salt concentration (100–500 ppm at 1.2 V). Experimental results reveal a strong positive correlation between voltage and desalination performance across all electrodes (Figs. 4d-e, S10a-c); higher voltages (≤1.2 V) consistently boost desalination capacity. Notably, capacity declined reversibly when voltage decreased from 1.2 to 0.8 V but fully recovered upon restoration to 1.2 V (Fig. 4d). This voltage-driven enhancement stems from increased electric field strength at the electrode-electrolyte interface, which accelerates Na^+ migration and adsorption kinetics [12]. Additionally, higher voltages improve active site utilization and ion accessibility, enhancing migration efficiency to achieve higher capacity and faster cycling response [50,64]. Note that elevated NaCl concentrations

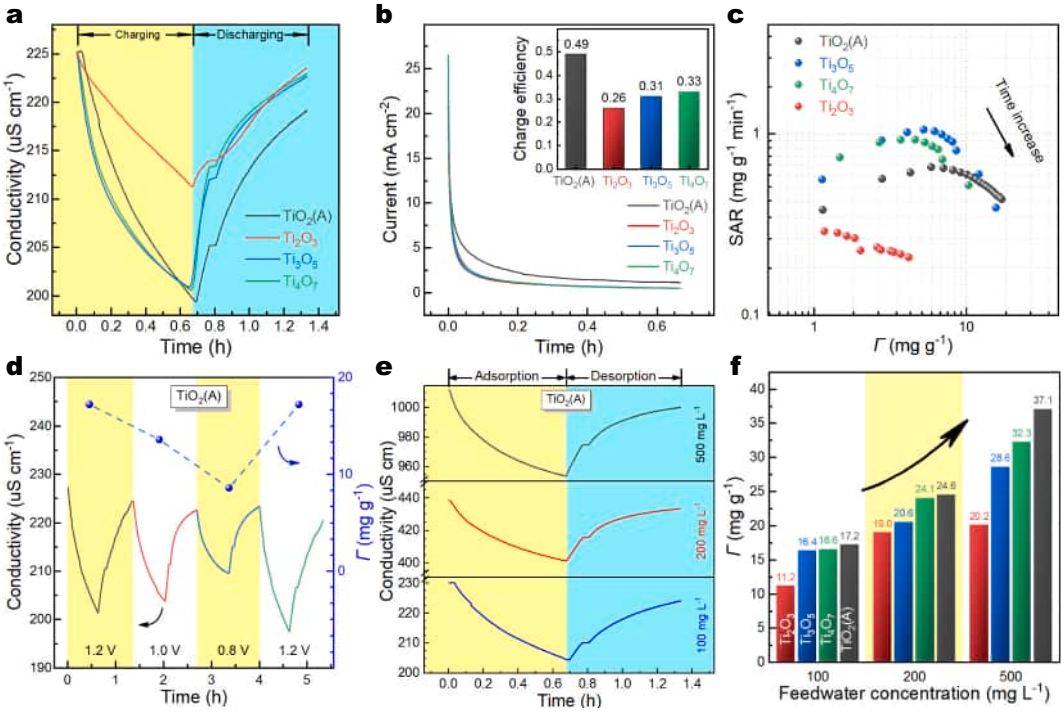

Fig. 4. Electrochemical desalination performance of the titanium (sub)oxide electrodes. (**a**) Conductivity profiles, and (**b**) the corresponding current density and charge efficiency (Λ) during the third HCDI cycle in 100 mg L^{-1} NaCl at 1.2 V; (**c**) Kim-Yoon analysis based on the data of panel **a** (100 mg L^{-1} NaCl, 1.2 V); (**d**) voltage-dependent conductivity profiles and adsorption capacity of the TiO_2(A) electrode in 100 mg L^{-1} NaCl; (**e**) concentration-dependent conductivity profiles of the TiO_2(A) electrode, and (**f**) concentration-dependent adsorption capacity (Γ) for these electrodes at 1.2 V.

significantly enhance charge-discharge kinetics (Figs. 4b, S10d-f), facilitating faster system equilibrium. Concurrently, the Γ values of the TiO_2(A) electrode exhibit strong concentration dependence (Fig. 4e), reaching 37.1 mg g^{-1} in 500 mg L^{-1} of NaCl solution, versus 24.8 mg g^{-1} (in 200 mg L^{-1}) and 17.2 mg g^{-1} (in 100 mg L^{-1}). All electrodes follow this trend (Fig. 4f), confirming a shared mechanism—electrostatic accumulation amplified by high ionic strength consistent with the capacitance analysis (Fig. 3c). Further, the titanium (sub)oxide electrodes demonstrate Γ values comparable to the state-of-the-art Ti-based electrodes applied to CDI (Table S2, Fig. S9b), underscoring the structure-driven desalination performance. Nonetheless, further rational optimization of these electrodes would be necessary for practical applications.

3.4. Recycling performance and potential mechanism

The durability of electrodes during repeated cycling plays a key role in shaping the potential applications of the materials. To assess the long-term stability of these titanium (sub)oxide electrodes used in HCDI, continuous charge-discharge cycling tests were conducted at 1.2 V in a 500 mg L^{-1} NaCl solution for a total of 40 cycles. As shown in Fig. S11, both the solution conductivity and the corresponding Γ curves exhibit a decreasing trend with increasing cycle numbers. This phenomenon indicates that the titanium (sub)oxide electrodes experience a certain degree of performance degradation over cycling. Specifically, the TiO_2(A) electrode exhibits the highest initial Γ of approximately 38.5 mg g^{-1} (Fig. 5a-b), which decreases gradually with cycle number and drops to 35.2 mg g^{-1} on the 40th cycle, achieving a Γ retention of 91.3 % and demonstrating excellent cycling stability. In contrast, the Ti_2O_3 electrode shows an initial Γ of ~20.8 mg g^{-1} with a Γ retention of 85.2 % (Fig. 5b). In parallel, Ti_3O_5 and Ti_4O_7 demonstrate increasing initial and final Γ values after 40 consecutive cycling relative to the Ti_2O_3 electrode. The Γ retention follows the order TiO_2(A) (91.3 %) > Ti_4O_7 (89.1 %) > Ti_2O_3 (85.2 %) > Ti_3O_5 (83.8 %), signifying the high recycling performance of all these titanium (sub)oxide electrodes.

Post-cycling structural characterizations (XRD, FTIR, EPR, and XPS) were used to elaborate the structure-performance relationship of these electrodes (Figs. 5c-f, S2d, S12-S14). For instance, the TiO_2(A) experiences clear structural degradation upon cycling as evidenced by the decline in XRD peak intensity, XPS peak intensity and the weakening of FTIR band (Ti—O) at 550–680 cm^{-1} (Figs. 5c-f, S12), which is believed to account for the loss of desalination capacity over cycling [28,29,36]. Notably, the loss of lattice oxygen is significant along with an increase in O_V (highlighted by the light-yellow shaded region) upon cycling, leading to increasing [O_V] from 0.18 up to 0.84 (Fig. 5e), which has also been verified by the EPR spectroscopy (Fig. S2d). One plausible mechanism for this observation is that while an appropriate Ov concentration is beneficial to desalination performance during the initial cycling stages, excessive cycling likely causes Ov to accumulate beyond a critical threshold, leading to irreversible structural damage. Concurrently, the Ti 2p splitting peaks showed a significant decrease in intensity and shifted toward higher energies due to irreversible surface oxidation after cycling, indicative of progressive corrosion and degradation of TiO_2(A). Specifically, cycling generates Ti^{3+} defects and oxygen vacancies, which, upon (incomplete) re-oxidation, lead to a more oxidized surface Ti environment than the original state, and thus a positive Ti 2p shift [65]. Similar phenomena recurred on both the Ti_3O_5 and Ti_4O_7 electrodes (Figs. S13, S14), indicating that they also suffered identical and irreversible structural degradation during cycling.

To ascertain the 'structure-performance' relationship, we have calculated the charge transfer rate constants (k_s, Table S1) and correlated them with their [O_V] values, C_s, and Γ (Fig. 6a-b). The k_s values show a well-defined positive dependence on [O_V], with a linear correlation coefficient (R^2) as high as 0.957 (Fig. 6a), implying an O_V-driven charge transfer mechanism inside the electrodes (Fig. 6c) [62,63]. In general, C_s and Γ exhibit a positive correlation (a high C_s leads to a high Γ), indicating that the electrode's charge storage capacity directly contributes to desalination performance [14,22]. Interestingly, this rule

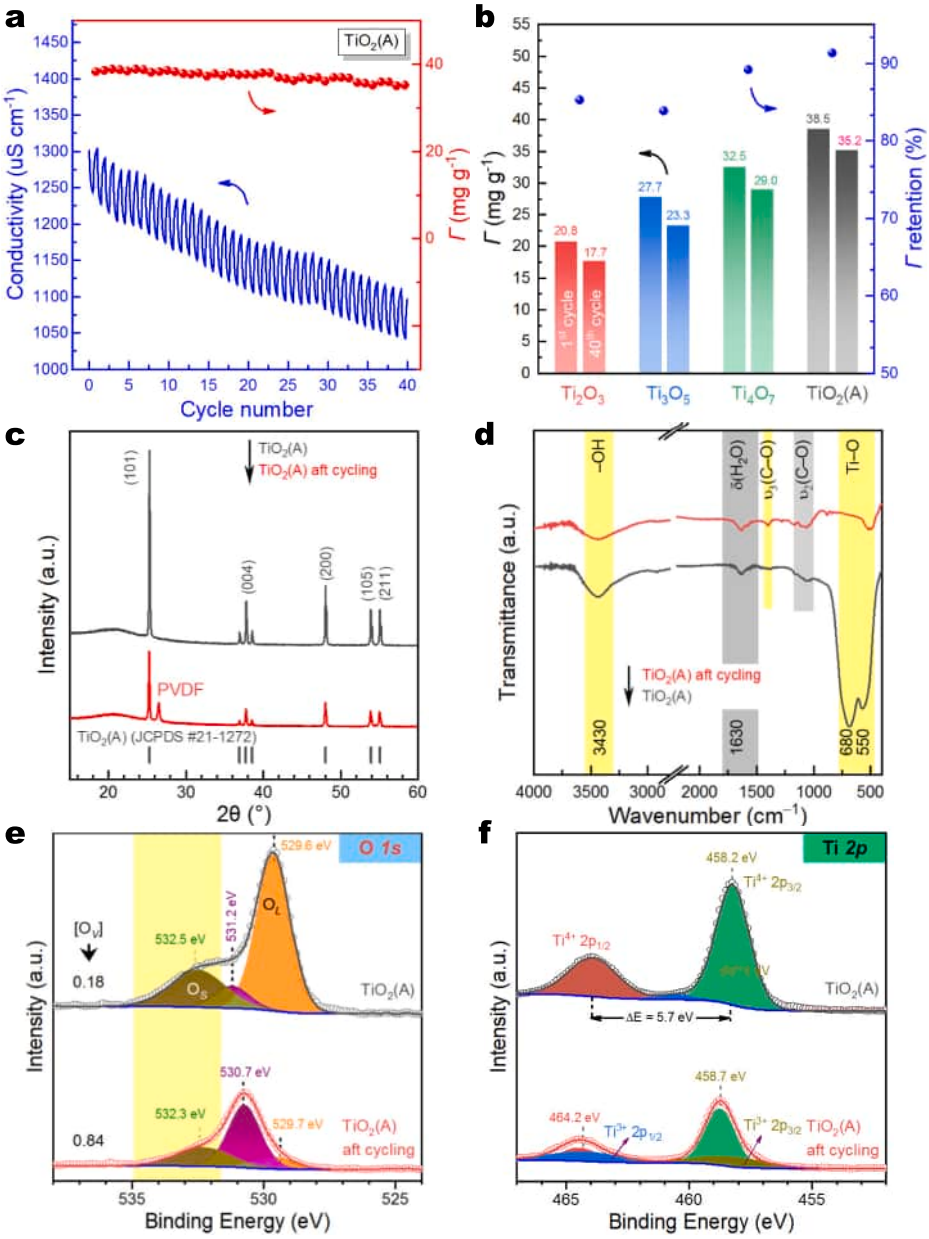

Fig. 5. (**a**) Cycling stability of TiO_2(A) electrodes, (**b**) comparison in Γ of the 1st and 40th cycle and the corresponding Γ retention of the titanium (sub)oxide electrodes in 500 mg L^{-1} of NaCl solution at 1.2 V; (**c**) XRD patterns, (**d**) FTIR spectra, (**e**, **f**) XPS spectra of (**e**) O 1 s (the light yellow shaded areas highlight the regions with significant spectral changes) and (**f**) Ti 2p regions of TiO_2(A) and the TiO_2(A) electrode after 40-cycle of consecutive charge-discharge operations in 500 mg L^{-1} of NaCl solution at 1.2 V. Note that the gradual decrease in solution conductivity over consecutive cycles in panel a is primarily attributed to the incomplete desorption of ions during the discharge step; while the decreases in XRD reflections and XPS peaks indicate the structural degeneration of the electrode, and the peak labeled with PVDF stems from the additive in the electrode preparation.

does not apply to these defect-rich titanium (sub)oxides (cf. Figs. 3e, 6b). This is likely attributed to both the crystallographic and the geometric properties of these (sub)oxides. Specifically, the larger particle sizes and agglomeration observed in these suboxides may pose ion/charge diffusion limitations compared with TiO_2(A) (Fig. 2b-d). Besides, the denser, shear-plane-dominated frameworks of Magnéli phases (including Ti_3O_5 and Ti_4O_7) offer a limited interstitial volume for Na^+ than the more open, structurally flexible TiO_2(A) framework [66,67]. Concurrently, a higher k_s does not guarantee a higher Γ (Fig. 6b), but lower k_s and lower C_s jointly lead to lower desalination capacity (i.e., Ti_2O_3). Essentially, other parameters, including crystal phase, particle size, pore geometry, conductivity, and rate capability, also play a critical role in determining the desalination performance [53,68,69]. For instance, TiO_2(A) exhibits faster charge/discharge rates and greater charge storage capacity through a pseudocapacitive mechanism when reduced to the nanoscale [68], exemplifying the nanoscale effect of the defect-rich titanium (sub) oxides in electrochemical energy storage and desalination. Recall that among the titanium (sub)oxides studied here, TiO_2(A) shows the smallest particle size (Fig. 2), which further offers charge storage and kinetics benefits relative to other titanium suboxides.

A recent theoretical study also showed that abundant O_V can effectively lower the adsorption energy barrier of Na^+ ions onto TiO_2 and is likely to provide more active sites, thereby enhancing Na^+ ion adsorption [33]. Nevertheless, future works are needed for correlating other parameters with desalination capacities and exploring the mechanism theoretically based on density function theory (DFT) calculations of Na^+ adsorption energies and diffusion pathways on surfaces with controlled O_V concentrations on a single phase, providing fundamental insights

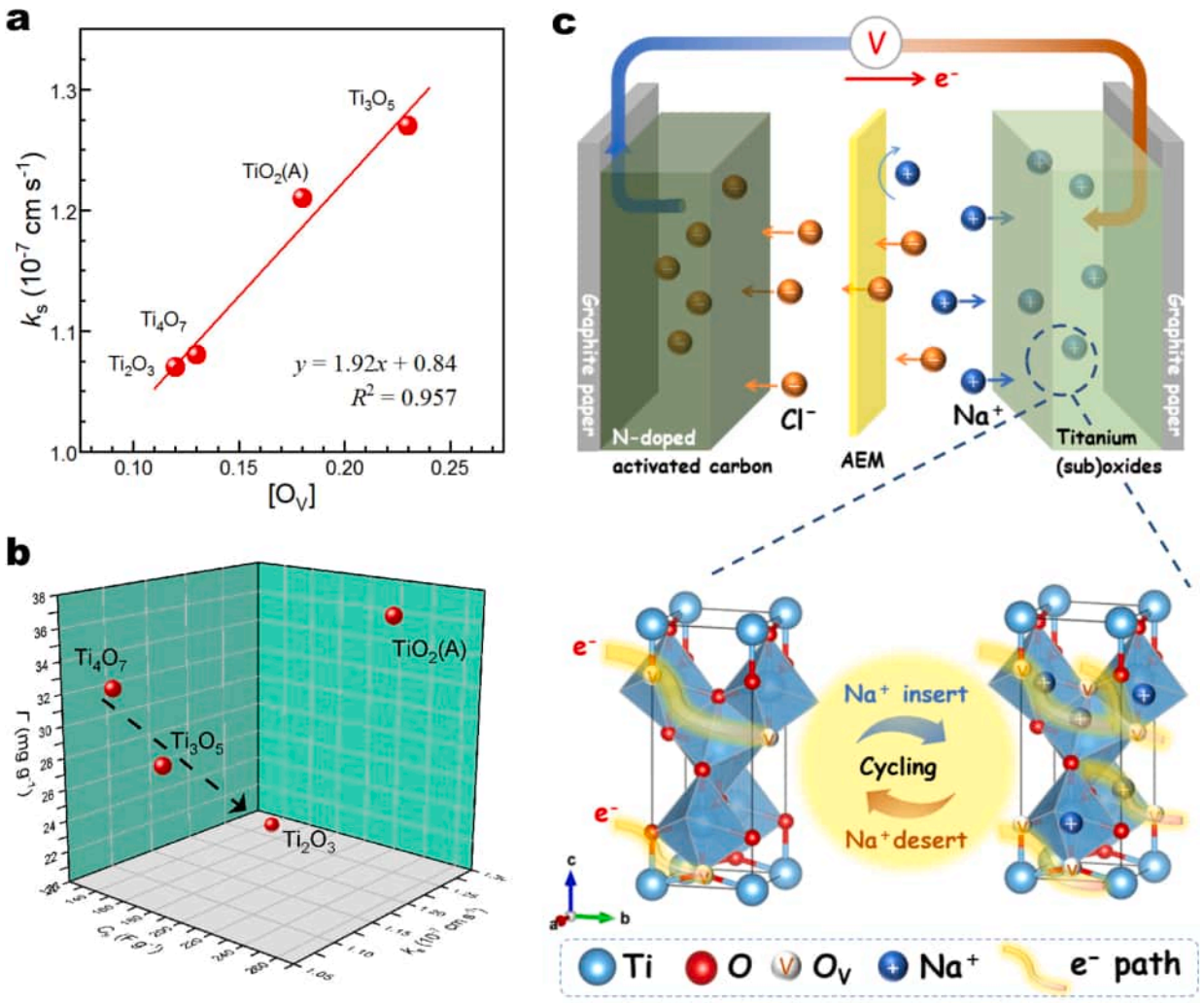

Fig. 6. (**a**) Correlation of [O_V] with the electrode transfer rate constants (k_s) of titanium (sub)oxide- electrodes; (**b**) correlation of [O_V] and specific capacitance (C_s) with Γ (in 500 mg L^{-1} of NaCl solution at 1.2 V) of the titanium (sub)oxide electrodes; (**c**) the proposed mechanism of the O_V-driven charge transfer pathways within the TiO_2(A) electrode during CDI operations.

into the 'structure-performance' relationship and the mechanisms for enhanced Na^+ capture. Collectively, the TiO_2(A) electrode demonstrates the superior desalination performance, which is probably attributed to its smaller particle size, higher specific capacitance, and a faster charge transfer rate driven by the oxygen vacancies.

4. Conclusions

This study systematically investigates the electrochemical properties and desalination performance of four titanium (sub)oxides (anatase TiO_2(A), Ti_2O_3, Ti_3O_5, Ti_4O_7) in a hybrid capacitive deionization (HCDI) system. Electrochemical characterization (CV, GCD, EIS) reveals TiO_2(A) achieves the highest specific capacitance (252.5 F g^{-1} at 0.3 A g^{-1}). Ti_3O_5, featuring the highest oxygen vacancies, exhibits the lowest charge transfer resistance and fastest interfacial ion kinetics among these titanium (sub)oxides. Desalination tests demonstrate TiO_2(A) attains a maximum salt adsorption capacity of 37.1 mg g^{-1} in 500 mg L^{-1} NaCl at 1.2 V, outperforming other oxides due to its open [TiO_6] octahedral framework and superior synergistic electron/ion transport synergy. TiO_2(A) also maintains robust performance across varying voltages and salt concentrations, coupled with optimal cycling stability attributed to its fine particle size, high capacitance, and fast charge transfer driven by abundant oxygen vacancies. While Ti_4O_7 shows moderately lower performance than TiO_2(A), it significantly surpasses Ti_2O_3 and Ti_3O_5, indicating good potential. Correlation analysis reveals an oxygen vacancy-driven charge transfer mechanism within these electrodes and dictates future investigations for elucidating the roles of other parameters and theoretical insights into the Na^+ capture mechanism. Collectively, defect-rich titanium (sub)oxides are promising HCDI electrode materials. This work elucidates structure-performance relationships in desalination and exemplifies an optimization strategy for oxygen vacancy-engineered electrodes, advancing electrochemical desalination technology.

CRediT authorship contribution statement

Pengcheng Yin: Writing – original draft, Validation, Investigation. **Yucheng Yang:** Investigation. **Shu Zhang:** Methodology. **Zhao Hu:** Investigation. **Dawei Li:** Resources, Project administration. **Feihu Li:** Writing – review & editing, Writing – original draft, Visualization, Supervision, Resources, Conceptualization.

Declaration of competing interest

The authors declare that they have no known competing financial interests or personal relationships that could have appeared to influence the work reported in this paper.

Acknowledgments

We are grateful to Dr. Qin at Nanjing University for XPS data collection, and to the anonymous referees for their insightful comments.

Appendix A. Supplementary data

Supplementary data to this article can be found online at https://doi.org/10.1016/j.cej.2025.171840.

Data availability

Data will be made available on request.

References

[1] M. Salehi, Global water shortage and potable water safety: today's concern and tomorrow's crisis, Environ. Int. 158 (2022) 106936, https://doi.org/10.1016/j.envint.2021.106936.
[2] J. Eliasson, The rising pressure of global water shortages, Nature 517 (2015) 6, https://doi.org/10.1038/517006a.
[3] M. Elimelech, W.A. Phillip, The future of seawater desalination: energy, technology, and the environment, Science 333 (2011) 712–717, https://doi.org/10.1126/science.1200488.
[4] G.D. Kang, Y.M. Cao, Development of antifouling reverse osmosis membranes for water treatment: a review, Water Res. 46 (2012) 584–600, https://doi.org/10.1016/j.watres.2011.11.041.
[5] S.M.J.S. Sabour, B. Ghorashi, A comprehensive review of major water desalination techniques and mineral extraction from saline water, Sep. Purif. Technol. 349 (2024) 127913, https://doi.org/10.1016/j.seppur.2024.127913.
[6] A. Alenezi, Y. Alabaiadly, Emerging technologies in water desalination: a review and future outlook, Energy Nexus 17 (2025) 100373, https://doi.org/10.1016/j.nexus.2025.100373.
[7] S. Porada, R. Zhao, A. van der Wal, V. Presser, P.M. Biesheuvel, Review on the science and technology of water desalination by capacitive deionization, Prog. Mater. Sci. 58 (2013) 1388–1442, https://doi.org/10.1016/j.pmatsci.2013.03.005.
[8] Y. Oren, Capacitive deionization (CDI) for desalination and water treatment - past, present and future (a review), Desalination 228 (2008) 10–29, https://doi.org/10.1016/j.desal.2007.08.005.
[9] K.G. Sun, M. Tebyetekerwa, C. Wang, X.F. Wang, X.W. Zhang, X.S. Zhao, Electrocapacitive deionization: mechanisms, electrodes, and cell designs, Adv. Funct. Mater. 33 (2023) 2213578, https://doi.org/10.1002/adfm.202213578.
[10] J. Lee, S. Kim, C. Kim, J. Yoon, Hybrid capacitive deionization to enhance the desalination performance of capacitive techniques, Energy Environ. Sci. 7 (2014) 3683–3689, https://doi.org/10.1039/c4ee02378a.
[11] T.T. Wu, G. Wang, S.Y. Wang, F. Zhan, Y. Fu, H.Y. Qiao, J.S. Qiu, Highly stable hybrid capacitive deionization with a MnO_2 anode and a positively charged cathode, Environ. Sci. Technol. Lett. 5 (2018) 98–102, https://doi.org/10.1021/acs.estlett.7b00540.
[12] J. Jin, Y. Bao, F.H. Li, Enhanced removal of Cu^{2+} and Pb^{2+} ions from wastewater via a hybrid capacitive deionization platform with MnO_2/N-doped mesoporous carbon nanocomposite electrodes, ACS Appl. Mater. Interfaces 17 (2025) 13783–13793, https://doi.org/10.1021/acsami.4c18755.
[13] S.Y. Wang, G. Wang, T.T. Wu, C.P. Li, Y.W. Wang, X. Pan, F. Zhan, Y.Q. Zhang, S. F. Wang, J.S. Qiu, Membrane-free hybrid capacitive deionization system based on redox reaction for high-efficiency NaCl removal, Environ. Sci. Technol. 53 (2019) 6292–6301, https://doi.org/10.1021/acs.est.9b00662.
[14] J. Jin, M. Li, M.T. Tang, Y. Li, Y.Y. Liu, H. Cao, F.H. Li, Phase- and crystallinity-tailorable MnO_2 as an electrode for highly efficient hybrid capacitive deionization (HCDI), ACS Sustain. Chem. Eng. 8 (2020) 11424–11434, https://doi.org/10.1021/acssuschemeng.0c04101.
[15] X.L. Zhou, S.R. Shu, X.Y. Ye, Z.J. Li, Engineering faradaic electrode materials for high-efficiency water desalination, Small 20 (2024) 2400047, https://doi.org/10.1002/smll.202400047.
[16] Y. Wang, Q.F. Pan, Y.X. Qiao, X.Y. Wang, D.F. Deng, F.H. Zheng, B. Chen, J.S. Qiu, Layered metal oxide Nanosheets with enhanced interlayer space for electrochemical deionization, Adv. Mater. 35 (2023) 2210871, https://doi.org/10.1002/adma.202210871.
[17] F. Yu, L. Wang, Y. Wang, X.J. Shen, Y.J. Cheng, J. Ma, Faradaic reactions in capacitive deionization for desalination and ion separation, J. Mater. Chem. A 7 (2019) 15999–16027, https://doi.org/10.1039/c9ta01264h.
[18] P. Srimuk, X. Su, J. Yoon, D. Aurbach, V. Presser, Charge-transfer materials for electrochemical water desalination, ion separation and the recovery of elements, Nat. Rev. Mater. 5 (2020) 517–538, https://doi.org/10.1038/s41578-020-0193-1.
[19] Y. Liu, K. Wang, X.T. Xu, K. Eid, A.M. Abdullah, L.K. Pan, Y. Yamauchi, Recent advances in faradic electrochemical deionization: system architectures versus electrode materials, ACS Nano 15 (2021) 13924–13942, https://doi.org/10.1021/acsnano.1c03417.
[20] D. Kang, C.H. Huang, M. Ding, H.Y. Yang, Review on the polymer materials for capacitive deionization, Desalination 586 (2024) 117884, https://doi.org/10.1016/j.desal.2024.117884.
[21] H. Wang, X.T. Xu, X.Y. Gao, Y.Q. Li, T. Lu, L.K. Pan, Design of three-dimensional faradic electrode materials for high-performance capacitive deionization, Coord. Chem. Rev. 510 (2024) 215835, https://doi.org/10.1016/j.ccr.2024.215835.
[22] Y. Bao, J. Jin, M.Y. Ma, M. Li, F.H. Li, Ion exchange conversion of Na-Birnessite to Mg-Buserite for enhanced and preferential Cu^{2+} removal via hybrid capacitive deionization, ACS Appl. Mater. Interfaces 14 (2022) 46646–46656, https://doi.org/10.1021/acsami.2c13086.
[23] D. Wei, B.X. Ouyang, Y.Y. Cao, L.J. Yan, B.C. Wu, P. Chen, T.Z. Zhang, Y.X. Jiang, H.Y. Wang, Coordination confined silver-organic framework for high performance electrochemical deionization, Adv. Sci. 11 (2024) 2401174, https://doi.org/10.1002/advs.202401174.
[24] P.J. Obeid, N. Sari-Chmayssem, P. Yammine, D. Homsi, H. El-Nakat, Z. Matar, S. Hamieh, D. Koumeir, A. Chmayssem, Designs and materials of electrodes for electrochemical sensors, Chemelectrochem 12 (2025) e202500230, https://doi.org/10.1002/celc.202500230.
[25] C.Z. Yuan, L.H. Su, B. Gao, X.G. Zhang, Enhanced electrochemical stability and charge storage of MnO_2/carbon nanotubes composite modified by polyaniline coating layer in acidic electrolytes, Electrochim. Acta 53 (2008) 7039–7047, https://doi.org/10.1016/j.electacta.2008.05.037.
[26] D.Y. Ma, X.R. Xue, M. Niu, Y.J. Wang, Q.Z. Luo, X.W. Zhu, H.L. Li, D.S. Wang, Improved Na^+ adsorption performance and storage mechanism of cobalt hexacyanoferrate/polyaniline composite during the hybrid capacitive deionization process, Sep. Purif. Technol. 348 (2024) 127804, https://doi.org/10.1016/j.seppur.2024.127804.
[27] M.W. Ryoo, J.H. Kim, G. Seo, Role of titania incorporated on activated carbon cloth for capacitive deionization of NaCl solution, J. Colloid Interface Sci. 264 (2003) 414–419, https://doi.org/10.1016/S0021-9797(03)00375-8.
[28] C. Kim, J. Lee, S. Kim, J. Yoon, TiO_2 sol-gel spray method for carbon electrode fabrication to enhance desalination efficiency of capacitive deionization, Desalination 342 (2014) 70–74, https://doi.org/10.1016/j.desal.2013.07.016.
[29] H.B. Li, Y.L. Ma, R. Niu, Improved capacitive deionization performance by coupling TiO_2 nanoparticles with carbon nanotubes, Sep. Purif. Technol. 171 (2016) 93–100, https://doi.org/10.1016/j.seppur.2016.07.019.
[30] M.W. Ryoo, G. Seo, Improvement in capacitive deionization function of activated carbon cloth by titania modification, Water Res. 37 (2003) 1527–1534, https://doi.org/10.1016/S0043-1354(02)00531-6.
[31] L. Zou, G. Morris, D. Qi, Using activated carbon electrode in electrosorptive deionisation of brackish water, Desalination 225 (2008) 329–340, https://doi.org/10.1016/j.desal.2007.07.014.
[32] D. Xu, Y.H. Gu, L. Chen, Y. Zhang, F. You, S.Y. Chen, C.L. Hu, H.B. Huang, J. Chen, MnO_2 Nanosheets on TiO_2 tetragonal prism Nanoarrays as electrode materials for electrochemical energy storage, ACS Appl. Nano Mater. 7 (2024) 22997–23007, https://doi.org/10.1021/acsanm.4c04173.
[33] Y.S. Xu, B.J. Chen, T. Jiang, H.J. Zhou, Rational in-situ construction of oxygen-deficient and carbon-coated TiO_2 hollow nanotubes for high-performance electrochemical desalination, Chem. Eng. J. 521 (2025) 166487, https://doi.org/10.1016/j.cej.2025.166487.
[34] D.W. Su, S.X. Dou, G.X. Wang, Anatase TiO_2: better anode material than amorphous and rutile phases of TiO_2 for Na-ion batteries, Chem. Mater. 27 (2015) 6022–6029, https://doi.org/10.1021/acs.chemmater.5b02348.
[35] M.N. Fan, Z.H. Lin, P. Zhang, X.D. Ma, K.P. Wu, M.L. Liu, X.H. Xiong, Synergistic effect of nitrogen and sulfur dual-doping endows TiO_2 with exceptional sodium storage performance, Adv. Energy Mater. 11 (2021) 2003037, https://doi.org/10.1002/aenm.202003037.
[36] M. Ding, S. Fan, S.Z. Huang, M.E. Pam, L. Guo, Y.M. Shi, H.Y. Yang, Tunable Pseudocapacitive behavior in metal-organic framework-derived TiO_2@porous carbon enabling high-performance membrane capacitive deionization, ACS Appl. Energy Mater. 2 (2019) 1812–1822, https://doi.org/10.1021/acsaem.8b01839.
[37] S.N. Misal, D.L. Li, S. Kim, B.P. Chaplin, Effect of solution conditions and applied potential on ion transport in TiO_2 Nanopores, ACS ES&T Eng. 4 (2024) 2495–2505, https://doi.org/10.1021/acsestengg.4c00295.
[38] C. Kim, S. Kim, J. Lee, J. Kim, J. Yoon, Capacitive and oxidant generating properties of black-colored TiO_2 nanotube Array fabricated by electrochemical self-doping, ACS Appl. Mater. Interfaces 7 (2015) 7486–7491, https://doi.org/10.1021/acsami.5b00123.
[39] H.F. Zhai, B.Y. Xia, H.S. Park, Ti-based electrode materials for electrochemical sodium ion storage and removal, J. Mater. Chem. A 7 (2019) 22163–22188, https://doi.org/10.1039/c9ta06713b.
[40] S. Nayak, B.P. Chaplin, Fabrication and characterization of porous, conductive, monolithic Ti_4O_7 electrodes, Electrochim. Acta 263 (2018) 299–310, https://doi.org/10.1016/j.electacta.2018.01.034.
[41] S. Garcia-Segura, X.L. Qu, P.J.J. Alvarez, B.P. Chaplin, W. Chen, J.C. Crittenden, Y. J. Feng, G.D. Gao, Z. He, C.H. Hou, X. Hu, G.B. Jiang, J.H. Kim, J.S. Li, Q.L. Li, J. Ma, J.X. Ma, A.B. Nienhauser, J.F. Niu, B.C. Pan, X. Quan, F. Ronzani, D. Villagran, T.D. Waite, W.S. Walker, C. Wang, M.S. Wong, P. Westerhoff, Opportunities for nanotechnology to enhance electrochemical treatment of pollutants in potable water and industrial wastewater - a perspective, Environ. Sci.-Nano 7 (2020) 2178–2194, https://doi.org/10.1039/d0en00194e.
[42] M.A. Alkhadra, X. Su, M.E. Suss, H.H. Tian, E.N. Guyes, A.N. Shocron, K. M. Conforti, J.P. De Souza, N. Kim, M. Tedesco, K. Khoiruddin, I.G. Wenten, J. G. Santiago, T.A. Hatton, M.Z. Bazant, Electrochemical methods for water purification, ion separations, and energy conversion, Chem. Rev. 122 (2022) 13547–13635, https://doi.org/10.1021/acs.chemrev.1c00396.
[43] Y.Q. Su, Z. Yu, R.A. Gu, W. Wu, S.L. Dai, S.A. Cheng, Blue hierarchical TiO_2 nanotube Array for significantly enhanced electrochemical oxidation performance

and stability of tetracycline degradation, ACS ES&T Eng. 3 (2023) 2222–2232, https://doi.org/10.1021/acsestengg.3c00164.
[44] S.A. Ekanayake, H.X. Mai, D.H. Chen, R.A. Caruso, Recent advances in synthesis and application of Magnéli phase titanium oxides for energy storage and environmental remediation, Chem. Sci. 16 (2025) 2980–3018, https://doi.org/10.1039/d4sc04477k.
[45] Y. Jing, S. Almassi, S. Mehraeen, R.J. LeSuer, B.P. Chaplin, The roles of oxygen vacancies, electrolyte composition, lattice structure, and doping density on the electrochemical reactivity of Magnéli phase TiO_2 anodes, J. Mater. Chem. A 6 (2018) 23828–23839, https://doi.org/10.1039/c8ta03719a.
[46] B. Bharti, S. Kumar, H.N. Lee, R. Kumar, Formation of oxygen vacancies and Ti^{3+} state in TiO_2 thin film and enhanced optical properties by air plasma treatment, Sci. Rep. 6 (2016) 32355, https://doi.org/10.1038/srep32355.
[47] S.S. Huang, Y.H. Lin, W. Chuang, P.S. Shao, C.H. Chuang, J.F. Lee, M.L. Lu, Y. T. Weng, N.L. Wu, Synthesis of high-performance titanium sub-oxides for electrochemical applications using combination of sol-gel and vacuum-Carbothermic processes, ACS Sustain. Chem. Eng. 6 (2018) 3162–3168, https://doi.org/10.1021/acssuschemeng.7b03189.
[48] X.Y. Xu, Y.L. Zheng, B. Gao, X.D. Cao, N-doped biochar synthesized by a facile ball-milling method for enhanced sorption of CO_2 and reactive red, Chem. Eng. J. 368 (2019) 564–572, https://doi.org/10.1016/j.cej.2019.02.165.
[49] G.X. Zhuang, Y.W. Chen, Z.Y. Zhuang, Y. Yu, J.G. Yu, Oxygen vacancies in metal oxides: recent progress towards advanced catalyst design, Sci. China-Mater. 63 (2020) 2089–2118, https://doi.org/10.1007/s40843-020-1305-6.
[50] S. Zhang, Z.N. Ye, M.Y. Ma, P.C. Yin, Y. Bao, F.H. Li, Optimizing the integration of nickel hexacyanoferrate with hollow mesoporous carbon spheres (HMCSs) for highly efficient capacitive deionization, Desalination 603 (2025) 118679, https://doi.org/10.1016/j.desal.2025.118679.
[51] Y. Bao, S.J. Miao, P.C. Yin, D.W. Li, F.H. Li, Optimization of NiHCF/MnO_2 composite electrodes for lithium extraction via capacitive deionization: a case of core-shell construction strategy, Chem. Eng. J. 525 (2025) 170471, https://doi.org/10.1016/j.cej.2025.170471.
[52] L.F. Heald, J.M. Garcia, S.G. Sayres, Oxygen deficiencies in titanium oxide clusters as models for bulk defects, J. Phys. Chem. A 126 (2022) 211–220, https://doi.org/10.1021/acs.jpca.1c07733.
[53] B.Q. Xu, H.Y. Sohn, Y. Mohassab, Y.P. Lan, Structures, preparation and applications of titanium suboxides, RSC Adv. 6 (2016) 79706–79722, https://doi.org/10.1039/c6ra14507h.
[54] C. Gomri, E. Makhoul, F.N. Koundia, E. Petit, S. Raffy, M. Bechelany, M. Semsarilar, M. Cretin, Electrochemical advanced oxidation combined to electro-Fenton for effective treatment of perfluoroalkyl substances "PFAS" in water using a Magnéli phase-based anode, Nanoscale Adv. 7 (2025) 261–268, https://doi.org/10.1039/d4na00626g.
[55] A.T. Bah, Z.Y. Shen, J.N. Yan, F.H. Li, Phosphorous recovery from water via batch adsorption enrichment combined with struvite crystallization in a fluidized bed reactor, J. Environ. Chem. Eng. 11 (2023) 110180, https://doi.org/10.1016/j.jece.2023.110180.
[56] F.H. Li, J. Jin, Z.Y. Shen, H.S. Ji, M. Yang, Y.M. Yin, Removal and recovery of phosphate and fluoride from water with reusable mesoporous Fe_3O_4@mSiO_2@mLDH composites as sorbents, J. Hazard. Mater. 388 (2020) 121734, https://doi.org/10.1016/j.jhazmat.2019.121734.
[57] L.T. Ye, M.Y. Zhang, P. Huang, G.C. Guo, M.C. Hong, C.S. Li, J.T.S. Irvine, K. Xie, Enhancing CO_2 electrolysis through synergistic control of non-stoichiometry and doping to tune cathode surface structures, Nat. Commun. 8 (2017) 14785, https://doi.org/10.1038/ncomms14785.
[58] Z.D. Zhang, B. Yang, L.Y. Chen, Z.L. Zhang, J.M. Guo, Oxygen vacancy-induced strengthening and toughening in (K,Na)NbO_3-based piezoceramics revealed via nanoindentation, Nat. Commun. 16 (2025) 7015, https://doi.org/10.1038/s41467-025-62424-3.
[59] P.V.R.K. Ramacharyulu, D.B. Nimbalkar, J.P. Kumar, G.K. Prasad, S.C. Ke, N-doped, S-doped TiO_2 nanocatalysts: synthesis, characterization and photocatalytic activity in the presence of sunlight, RSC Adv. 5 (2015) 37096–37101, https://doi.org/10.1039/c4ra08858a.
[60] J.Z. Xie, J.X. Ma, C.Y. Zhang, X.T. Kong, Z.W. Wang, T.D. Waite, Effect of the presence of carbon in Ti_4O_7 electrodes on anodic oxidation of contaminants, Environ. Sci. Technol. 54 (2020) 5227–5236, https://doi.org/10.1021/acs.est.9b07398.
[61] M. Nagao, S. Misu, J. Hirayama, R. Otomo, Y. Kamiya, Magneli-phase titanium suboxide nanocrystals as highly active catalysts for selective Acetalization of furfural, ACS Appl. Mater. Interfaces 12 (2020) 2539–2547, https://doi.org/10.1021/acsami.9b19520.
[62] Z.K. Hao, J. Lyu, M. Tian, X. Zhang, K.X. Wang, S.W. Yang, Y.X. Zhang, G.Q. Xu, Unraveling the synergistic effects of oxygen vacancy and amorphous structure on TiO_2 for high-performance Lithium storage, Small Struct. 5 (2024) 2300442, https://doi.org/10.1002/sstr.202300442.
[63] W. Song, H.G. Zhao, J.Q. Ye, M.M. Kang, S.Y. Miao, Z. Li, Pseudocapacitive Na^+ insertion in Ti-O-C channels of TiO_2-C nanofibers with high rate and Ultrastable performance, ACS Appl. Mater. Interfaces 11 (2019) 17416–17424, https://doi.org/10.1021/acsami.9b02123.
[64] S.J. Miao, P.C. Yin, S. Zhang, Z.J. Zhang, D.W. Li, F.H. Li, Boosting enhanced capacitive deionization of H_2TiO_3/carbon electrodes by yolk-shell construction, Water Res. 289 (2026) 124785, https://doi.org/10.1016/j.watres.2025.124785.
[65] C. Yan, Y. Liao, C.J. Shen, X.F. Weng, R.L. Lei, C.L. Liao, Y.X. Zhou, M. Wang, Uranium extraction by a graphene-based asymmetric electrode configuration through combined complexation, electro-adsorption, and photocatalytic reduction, Chem. Eng. J. 461 (2023) 142012, https://doi.org/10.1016/j.cej.2023.142012.
[66] Q.L. Wei, X.Q. Chang, D. Butts, R. DeBlock, K. Lan, J.B. Li, D.L. Chao, D.L. Peng, B. Dunn, Surface-redox sodium-ion storage in anatase titanium oxide, Nat. Commun. 14 (2023) 7, https://doi.org/10.1038/s41467-022-35617-3.
[67] G.W. Lee, B.H. Park, M. Nazarian-Samani, Y.H. Kim, K.C. Roh, K.B. Kim, Magneli phase titanium oxide as a novel anode material for potassium-ion batteries, ACS Omega 4 (2019) 5304–5309, https://doi.org/10.1021/acsomega.9b00045.
[68] J. Wang, J. Polleux, J. Lim, B. Dunn, Pseudocapacitive contributions to electrochemical energy storage in TiO_2(anatase) nanoparticles, J. Phys. Chem. C 111 (2007) 14925–14931, https://doi.org/10.1021/jp074464w.
[69] D. Dambournet, I. Belharouak, K. Amine, Tailored preparation methods of TiO_2 Anatase, rutile, Brookite: mechanism of formation and electrochemical properties, Chem. Mater. 22 (2010) 1173–1179, https://doi.org/10.1021/cm902613h.